

Structural and morphological properties of $\text{Ce}_{(1-x)}\text{Fe}_x\text{O}_{2-\delta}$ synthesized by citrate route

Mariano O. Mazan^a, Aldo F. Craievich^b, Emilia B. Halac^{c,d}, Márcia C.A. Fantini^b,
Diego G. Lamas^{d,e}, Susana A. Larrondo^{f,g,*}

^aDepartamento de Ingeniería Química, Facultad de Ingeniería, Universidad de Buenos Aires, Pabellón de Industrias, Ciudad Universitaria, 1428 Buenos Aires, Argentina

^bInstituto de Física, Universidade de São Paulo, Travessa R da Rua do Matão, No. 187, Cidade Universitária, 05508-900 São Paulo, Brazil

^cDepartamento de Física, Centro Atómico Constituyentes, Av. Gral. Paz 1499, 1650 San Martín, Pcia. de Buenos Aires, Argentina

^dEscuela de Ciencia y Tecnología, UNSAM, Campus Miguelete, 25 de Mayo y Francia, 1650 San Martín, Provincia de Buenos Aires, Argentina

^eConsejo Nacional de Investigaciones Científicas y Técnicas, Argentina

^fCINSO (Centro de Investigaciones en Sólidos), CITEDEF-UNIDEF-CONICET, J.B. de La Salle N 4397, 1603 Villa Martelli, Pcia. de Buenos Aires, Argentina

^gInstituto de Investigación e Ingeniería Ambiental, UNSAM, Campus Miguelete, 25 de Mayo y Francia, 1650 San Martín, Provincia de Buenos Aires, Argentina

Received 12 July 2015; received in revised form 2 August 2015; accepted 6 August 2015

Available online 14 August 2015

Abstract

Cerium-based materials were intensively studied in last years because of their high oxygen storage capacity (OSC) associated to the reversible $\text{Ce}^{4+} \leftrightarrow \text{Ce}^{3+}$ process and their properties closely related to the defect chemistry that could be adjusted by adequate selection of dopant. Fe^{3+} cation, due to its effective ionic radius smaller than that of Ce^{4+} , is an interesting doping agent. In this work we present the synthesis and characterization of $\text{Ce}_{(1-x)}\text{Fe}_x\text{O}_{2-\delta}$ mixed oxides ($0 \leq x \leq 1$) synthesized by the so named “citrate method”. Our X-ray diffraction results suggest a rather strong dependence of lattice parameter on nanocrystal size, while Raman spectroscopy evidenced the formation of a small volume fraction of hematite clusters in samples with relatively high iron content, $x \geq 0.15$, not observable in X-ray diffraction experiments. The solid solutions exhibit high porosity and specific surface area, with nearly 10% of pore volume in the micropore size range, making these materials potentially useful for applications in catalysis.

© 2015 Elsevier Ltd and Techna Group S.r.l. All rights reserved.

Keywords: Citrate synthesis; Iron doped ceria; Scanning electron microscopy; X-ray diffraction; Raman spectroscopy

1. Introduction

Cerium-based solid solutions have been intensively studied in the last years because of their high oxygen storage capacity (OSC) associated to the reversible $\text{Ce}^{4+} \leftrightarrow \text{Ce}^{3+}$ process. The fluorite-like structure of CeO_2 -based materials has an exceptional tolerance to host large amounts of oxygen-ion vacancies introduced by dopants or by reduction processes (such as

Ce^{4+} to Ce^{3+}). Besides, these oxygen vacancies are rapidly refilled via Ce^{3+} reoxidation when exposed to an oxidizing atmosphere [1]. Doped cerium oxides have been synthesized for many applications such as photocatalysts [2], UV rays blockers [3], oxygen sensors [4], fuel cells materials [5], catalysts for many applications like three-way converters [6], removal of arsenic from water [7], carbon dioxide hydrogenation [8], water gas shift reaction [9], CO preferential oxidation [10], partial oxidation of methane [11], and many others.

The properties of ceria-based materials are closely related to their defect chemistry, which is mainly determined by the concentration, size and charge of the dopant cation [12]. Many cations have been tested as dopants such as Zr^{4+} [6], Gd^{3+} and Sm^{3+} [13] among others. It was established that

*Corresponding author at: CINSO (Centro de Investigaciones en Sólidos), CITEDEF-UNIDEF-CONICET, J.B. de La Salle N 4397, 1603 Villa Martelli, Pcia. de Buenos Aires, Argentina. Tel.: +54 11 47098158.

E-mail addresses: slarrondo@citedef.gob.ar,
slarrondo@unsam.edu.ar (S.A. Larrondo).

doping of ceria with isovalent cations with sizes lower than that of Ce ions, such as Zr^{4+} , increases the OSC by decreasing the energy barrier for reduction from Ce^{4+} to Ce^{3+} [14]. On the other hand, doping with aliovalent cations, such as Gd^{3+} , diminishes the migration barrier of the diffusion of oxygen ions through the cerium oxide matrix [1]. In the present investigation we are particularly interested in the study of the structural effects associated to the incorporation of M^{3+} cations into the crystalline structure of CeO_2 .

Fe^{3+} seems to be a good candidate as a M^{3+} cation to be added to ceria because iron is the most abundant metal in the earth's crust and is cheaper than other elements such as Gd or Sm. Notice that Fe^{3+} is a trivalent cation with an effective ionic radius equal to 0.69 Å in a six coordination structure, which is much lower than the ionic radius of Ce^{4+} in an eight coordination number (1.11 Å) [15].

It was established that when the ceria-based solid solution is prepared by solid state reaction, iron exhibits a very low solubility limit (< 1 mol%) [16]. However, the synthesis of Ce–Fe mixed oxides through mild synthesis processes – yielding small particles on the nanoscale range – could be successfully applied to stabilize a rather high amount of iron embedded in ceria structures. Ce–Fe mixed oxides with high iron content are expected to exhibit interesting properties potentially useful for a wide scope of applications.

Many authors have synthesized $\text{Ce}_{1-x}\text{Fe}_x\text{O}_{2-\delta}$ solids by using different synthesis methods such as hydrothermal processes [12], co-precipitation [17], forced hydrolysis [18], sol gel [19] and microemulsion [20], among others [21]. However, controversies still remain regarding the dependence of lattice parameter on concentration, the limit of iron solubility and the specific locations of iron cations, in substitutional and/or interstitial sites of the host matrix.

In the present work we describe a process of synthesis of Ce–Fe mixed oxides by the citrate synthesis route with Ce/Fe atomic ratios from 0/1 to 1/0. The obtained powdered materials were characterized by high resolution field emission scanning electron microscopy (FESEM) with energy dispersive X-ray spectroscopy (EDS), adsorption–desorption of nitrogen at its normal boiling point (77 K), small-angle X-ray scattering (SAXS), X-ray diffraction (XRD) and Raman spectroscopy. Using these techniques, the limit of solubility, dependence of iron content on the lattice parameter, vacancy generation, crystallite sizes, porosity structures and specific surface areas are analyzed.

2. Experimental

2.1. Synthesis

A number of $\text{Ce}_{(1-x)}\text{Fe}_x\text{O}_{2-\delta}$ mixed oxides with different Fe to Ce atomic ratios were synthesized by the citrate method. The different samples to be studied had iron contents equal to 0, 0.05, 0.10, 0.15, 0.20, 0.30, 0.50, 0.70 and 1 (at%). These samples are named as 0Fe, 5Fe, 10Fe, 15Fe, 20Fe, 30Fe, 50Fe, 70Fe and 100Fe, respectively.

The amounts of $\text{Ce}(\text{NO}_3)_3 \cdot 6\text{H}_2\text{O}$ (Sigma-Aldrich, 99.99%) and $\text{Fe}(\text{NO}_3)_3 \cdot 9\text{H}_2\text{O}$ (Sigma-Aldrich, 99.99%) to obtain the nominal compositions mentioned above were dissolved in 50 cm³ of bi-distilled water. The so-obtained solutions were stirred until complete dissolution of metal nitrates. Citric acid ($\text{C}_6\text{H}_8\text{O}_7 \cdot \text{H}_2\text{O}$, Merck, 99.5%) was added, in acid to metal ions molar ratios 1:1 under continuous stirring until complete dissolution. The solution was placed in an open vessel, heated up to 363 K and kept at this temperature in order to evaporate the water. After 17 h, the formed gel was softly crushed, without removing it from the vessel, and kept at 363 K for one more hour. Afterwards, the temperature was slowly raised up in order to trigger the auto ignition process which proceeded very fast, with formation of bright and yellowish flames indicating very high temperature. After the end of the ignition, the powder was allowed to cool down to room temperature. After that, it was transferred to crucibles and calcined at 623 K during two hours.

2.2. Characterization techniques

FESEM and EDS analyses were performed by using a Zeiss Supra 40 instrument. The powdered samples were placed onto an adhesive carbon-filled conductive tape in order to avoid electric charging.

The N_2 physisorption isotherms (adsorption and desorption) were obtained with a Quantachrome Autosorb Automated Gas Sorption System, at the nitrogen normal boiling temperature (77 K). The samples were degassed at 323 K for 17 h. The specific surface area was calculated by applying the Brunauer, Emmett and Teller (BET) method, with the adsorption isotherm in the range of relative pressures below 0.3. Pore volume and size distribution in the mesopore range (2–50 nm) were determined by using the Barrett–Joyner–Halenda model (BJH) applied to the desorption isotherm. The micropore volume was evaluated by applying the Dubinin–Radushkevich (DR) equation in the very low partial pressure region of isotherm Eq. (1) [22]:

$$\frac{W}{W_0} = e^{-(RT \ln(x)/E)^2} \quad (1)$$

where W is the total mass of adsorbed nitrogen, W_0 the mass adsorbed in micropores and x the relative pressure (p/p_0). Plotting $\ln(W)$ versus $(\ln(x))^2$ a straight line is expected, with $(RT/E)^2$ as slope and $\ln(W_0)$ as the interception obtained by extrapolating to $(\ln(x))^2 \rightarrow 0$. From this latter value the volume of micropores is obtained.

SAXS measurements were performed using Bruker NanoStar setup, with Cu K α radiation ($\lambda = 1.5418$ Å). The X-ray beam was collimated by a set of Gobbel mirrors and 3 pinholes to obtain a point-like beam cross-section. The powdered samples were enclosed in a cell between two thin mica windows. The beam path from the X-ray source to the X-ray detector was maintained under rough vacuum ($\sim 10^{-2}$ Torr). The SAXS patterns were recorded with a Vantec 2D photon detector during 2 h of counting time. The parasitic scattering intensity produced by mica windows and collimating slits was determined and properly

subtracted. Since the dimension of the beam cross-section and the sizes of the pixel are very small, no mathematical desmearing processing was applied to the experimental SAXS curves. The final SAXS curves were analyzed by applying GNOM software [23,24]. The analysis of SAXS results allow to characterize the nanoporous structure of the samples.

XRD experiments were performed using a Rint Ultima+ Rigaku equipment with Bragg–Brentano geometry. The diffraction patterns were collected in a 2θ scan range from 20° to 135° , with 0.02° step and 5 s counting-time, using Cu K α radiation ($\lambda=1.5418$ Å). The lattice parameters were obtained by applying Rietveld refinement to XRD patterns using the FullProf program (Windows version, September 2012) [25]. The average crystallite sizes were determined by applying the Scherrer equation [26]. The profile of the (111) Bragg peak – which is the most intense XRD peak for the fluorite-type structure – was selected for this calculation.

Raman spectra were recorded with a LabRAM HR Raman system (Horiba Jobin Yvon), equipped with two monochromator gratings and a charge coupled device detector. An 1800 g/mm grating and a 100 μ m hole resulted in a spectral resolution of 1.5 cm^{-1} . The spectrograph is coupled to an imaging microscope with $10\times$, $50\times$, and $100\times$ magnifications. The He–Ne laser line at 632.8 nm was used as excitation source. Several measurements were performed, adjusting the laser fluence, to ensure minimal heating and no alteration of sample. Measurements were carried out using a backscattering geometry, with $50\times$ and $100\times$ magnifications.

3. Experimental results

3.1. FESEM and EDS

FESEM images of powdered samples with different Fe contents are shown in Fig. 1. All pictures exhibit the presence of very small crystallites agglomerated in large particles. Particularly, the images corresponding to samples 5Fe, 10Fe, 15Fe, 20Fe and 30Fe evidence nanocrystals agglomerated in planar sheet-like particles. Micrographs of samples 15Fe and 20Fe show micro- and macro- intra-particle pores, while in sample 30Fe particles showed more compact planar particles with slit-like pores inside. Images associated to samples with higher iron content exhibit more agglomerated particles and less porosity. Pure CeO₂ (sample 0Fe) exhibits the presence of very small crystallites and a porous structure while pure iron oxide (sample 100Fe) nanocrystals agglomerated in a very compact morphology, with a very low amount of pores. Therefore, the increment of iron content favors loss of intra-particle porosity.

All compositions determined from EDS analysis are similar to the nominal values, with deviations not larger than 1 at%. The EDS images also suggest a uniform composition of the three atomic species (Ce, Fe and O).

3.2. N₂ physisorption

In Fig. 2 the nitrogen adsorption–desorption isotherms at 77 K corresponding to all studied samples are displayed together. The

isotherms of samples 0Fe–50Fe and 100Fe are type IV according to IUPAC classification, with the typical hysteresis loop in the 0.4–0.99 relative pressure range associated to the existence of mesopores, while sample 70Fe has an isotherm that could be classified as type I with a very narrow hysteresis loop. Thus, in this last case a smaller amount of mesopores is expected [22]. The curvature observed in the relative pressure range below 0.1 suggests the existence of micropores.

Textural characterization results obtained from nitrogen adsorption–desorption isotherms are summarized in Table 1. We have also reported in Table 1 the agglomeration ratio ($D_{\text{BET}}/D_{\text{XRD}}$), where D_{XRD} is the average crystallite size calculated from XRD results that will be reported later.

BET specific surface area (S_{BET}) of Ce_(1-x)Fe_xO_{2- δ} samples are similar or even larger than those reported by previous authors [20,27–29]. Some authors observed a maximum in BET area for small concentration of Fe followed by a continuous decrease for increasing iron content [20,27]. Other researchers observed a monotonic decrease in specific surface area for increasing iron doping [29]. Our results reported in Table 1 indicate that excepting the sample 10Fe all others exhibit a clearly increasing trend for increasing iron content with a maximum for sample 70Fe.

The experimental results concerning pore volume (total, micro- and meso-pores volume) shows an oscillatory behavior without a well-defined trend.

3.3. SAXS measurements

In order to achieve a complementary description of micropore size distribution, another type of characterization by applying the SAXS method was performed. As expected all SAXS 2D patterns produced by the different powdered samples are isotropic. In Fig. 3, the SAXS intensities $I(q)$, corresponding to all studied samples, are displayed as functions of the modulus of scattering vector (q). In order to obtain additional information about the pore size distribution in the studied samples, we have assumed a very simple model, where the pores with radii in the 0–20 nm range are spherical and not spatially correlated. The SAXS curves were analyzed by applying the GNOM package [23,24]. The results plotted in Fig. 3 show that modeled curves derived from GNOM (solid lines) are in very good agreement with experimental SAXS curves (symbols). The output from GNOM program yielded the volume weighted radius distribution functions, $V(R)$, displayed in Fig. 4.

The features of the volume weighted radius distributions indicate the presence of a wide range of pore sizes in samples 0Fe–30Fe, with a maximum at about $R\sim 3.0$ nm. Samples 50Fe and 70Fe show a narrow distribution in the 0–5 nm region, centered in 2 nm, in agreement with the more agglomerated particles and loss of porosity observed in SEM images.

3.4. X-ray diffraction: composition dependence of lattice parameter and average crystallite size

XRD patterns of all studied powders are displayed in Fig. 5a. For iron doping from 0 up to 30 at% only the Bragg peaks

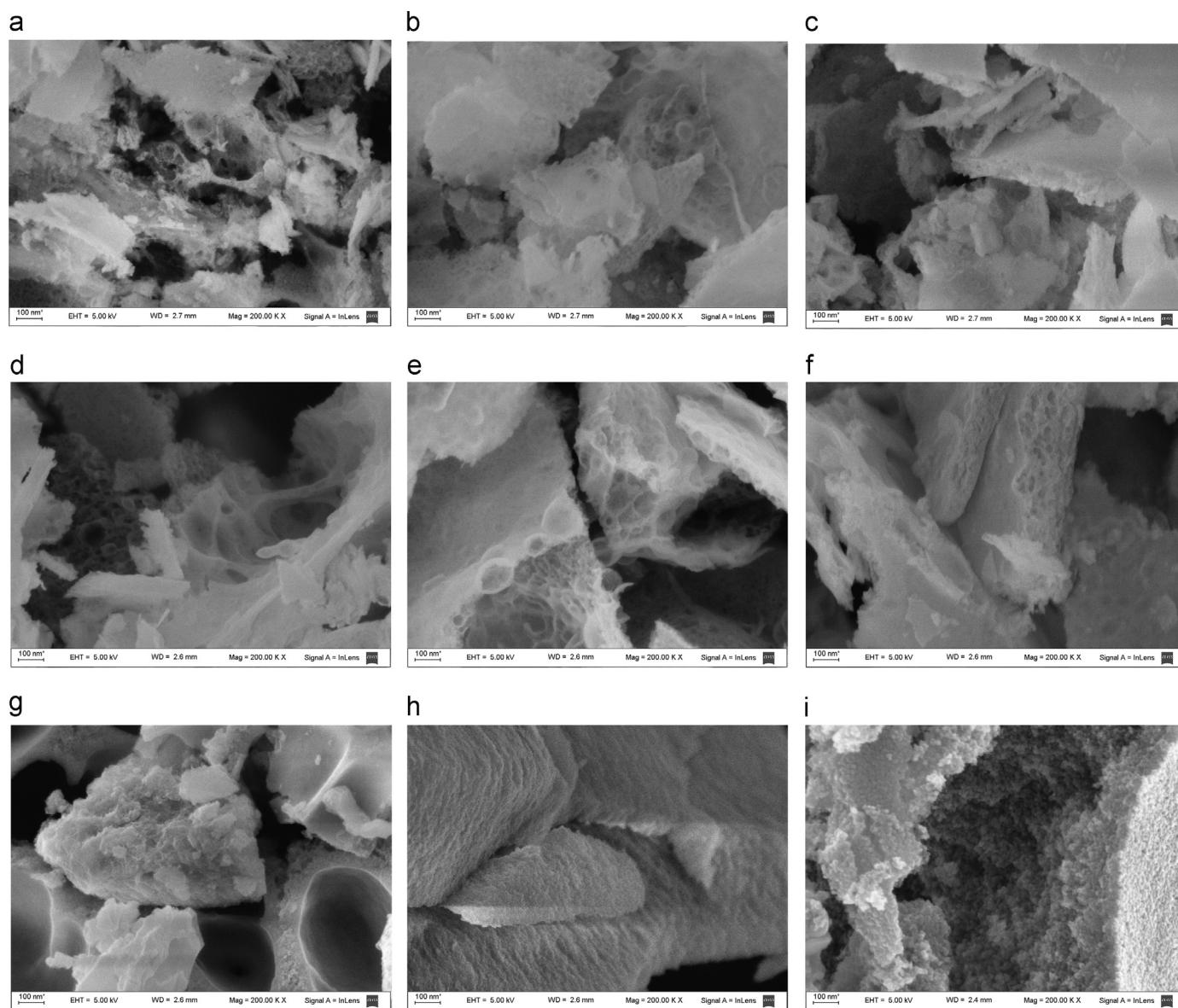


Fig. 1. Scanning electron microscopy images corresponding to all studied samples.(a) 0Fe; (b) 5Fe; (c) 10Fe; (d) 15Fe; (e) 20Fe; (f) 30Fe; (g) 50Fe; (h) 70Fe; (i) 100Fe.

corresponding to the cubic fluorite-type structure (fcc lattice) of cerium oxide are apparent in XRD patterns. The diffraction patterns of solid solutions with higher iron content indicate the segregation of α - Fe_2O_3 and Fe_3O_4 . In Fig. 5b an enlargement of the 2θ range associated to Bragg peaks (111) and (200) of fluorite structure is depicted. The diffraction peaks exhibit a progressive shift toward high 2θ angles for increasing iron content, thus indicating changes in interplanar distances and contraction of the structure. This trend is a priori expected because iron cations have smaller sizes than cerium cations. All Bragg peaks associated to samples 0Fe, 5Fe, 10Fe, 15Fe and 20Fe are symmetric while diffraction peaks corresponding to sample 30Fe exhibits a weak asymmetry which is probably related to the existence of some inhomogeneity in composition and/or structure.

The X-ray patterns of monophasic samples corresponding to iron contents up to 30% were refined by the Rietveld method. The spatial group $Fm\bar{3}m$ corresponding to the basic fluorite-type

structure of pure cerium oxide was assumed, with the iron atoms substituting cerium host positions. The refined lattice parameters and the conventional R_p , R_{wp} and χ^2 Rietveld quality factors are reported in Table 2. The lattice parameter as function of Fe content displayed in Fig. 6a indicate an oscillatory behavior with a general decreasing trend for increasing iron doping. The lattice parameter decreases for increasing Fe content from 0 up to 15 at %, while for an increment in iron doping from 10 to 15 at%, the lattice parameter increases. A decreasing trend is again apparent for further increments in iron content up to 30 at%. Further explanation about the observed variation of lattice parameter will be given in Section 4.

The average crystallite sizes of monophasic samples determined by the Scherrer equation are plotted in Fig. 6b. All samples are composed of crystals in the nanoscale range, being the largest that of pure ceria, with an average size $D_{\text{XRD}} = 7.1$ nm, and the smallest that of sample 30Fe, with $D_{\text{XRD}} = 4.0$ nm.

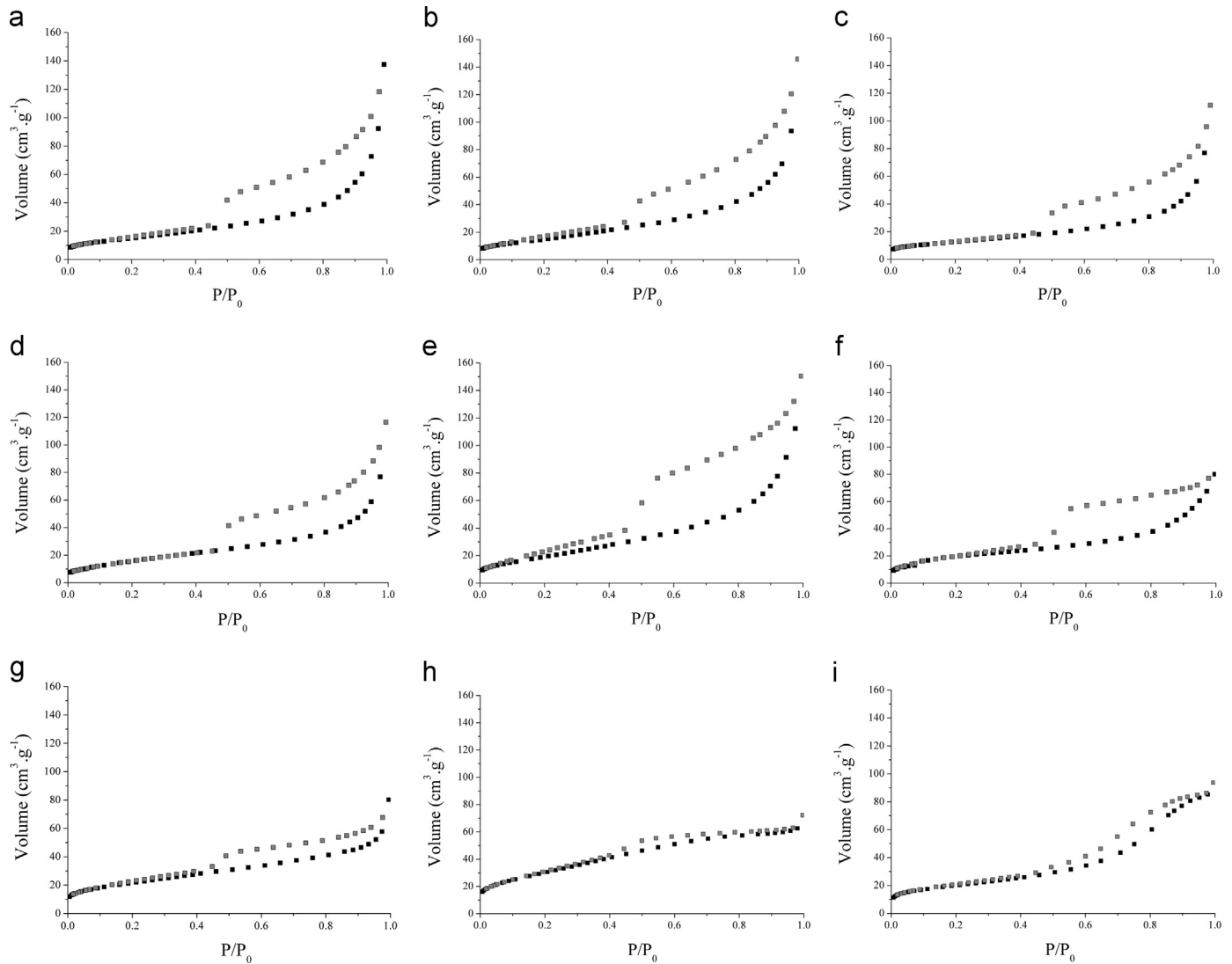


Fig. 2. Adsorption and desorption of nitrogen at 77 K for (a) 0Fe; (b) 5Fe; (c) 10Fe; (d) 15Fe; (e) 20Fe; (f) 30Fe; (g) 50Fe; (h) 70 Fe; (i) 100Fe.

Table 1
Textural characterization derived from nitrogen adsorption-desorption isotherms.

Sample	S_{BET} (m^2/g)	Total pore volume (cm^3/g)	Micropore volume calculated by DR (cm^3/g)	Mesopore volume calculated by BJH (cm^3/g)	Average micropore diameter (nm)	D_{BET}^{**} (nm)	$D_{\text{BET}}/D_{\text{XRD}}$
0Fe	55	0.21	0.020	0.19	2.3	15.1	2.1
5Fe	58	0.23	0.019	0.20	2.2	14.7	2.8
10Fe	46	0.17	0.017	0.15	2.2	19.0	3.7
15Fe	61	0.18	0.018	0.17	2.2	14.8	2.4
20Fe	74	0.23	0.024	0.23	2.4	12.6	2.25
30Fe	78	0.12	0.026	0.13	2.6	12.4	3.1
50Fe	78	0.12	0.029	0.11	2.3	*	*
70Fe	112	0.11	0.041	0.10	2.4	*	*
100Fe	71	0.15	0.030	0.14	2.4	*	*

*Multiphased sample.

** $D_{\text{BET}} = 6(S_{\text{BET}}\rho)^{-1}$; D_{XRD} : average crystallite size obtained by applying Scherrer equation.

3.5. Raman spectra

Raman results are displayed in Figs. 7 and 8. The main peak observed in Fig. 7 for all samples at 460 cm^{-1} is assigned to the F_{2g} Raman active mode in metal dioxides with a fluorite-like structure [17,30], corresponding to cerium oxide (CeO_2). A shift of this peak toward lower frequencies for increasing iron content is apparent in Fig. 7. This shift can be assigned to the reduction in crystallite size [17]. Weak peaks at 260 cm^{-1} and 590 cm^{-1} are apparent in Fig. 8, which are second order peaks associated to a transverse mode and to oxygen-ion vacancies in the cerium oxide lattice, respectively [27]. The observed relative increasing area of peak at 590 cm^{-1} with respect to that of the peak at 460 cm^{-1} , for increasing iron content indicates that iron atoms are incorporated into the fluorite lattice structure increasing the number of oxygen-ion vacancies.

Besides, in Fig. 8 two peaks at 215 cm^{-1} and 290 cm^{-1} associated to the structure of hematite (Fe_2O_3) [28,31–33] are clearly visible, while a very weak signal is observed at

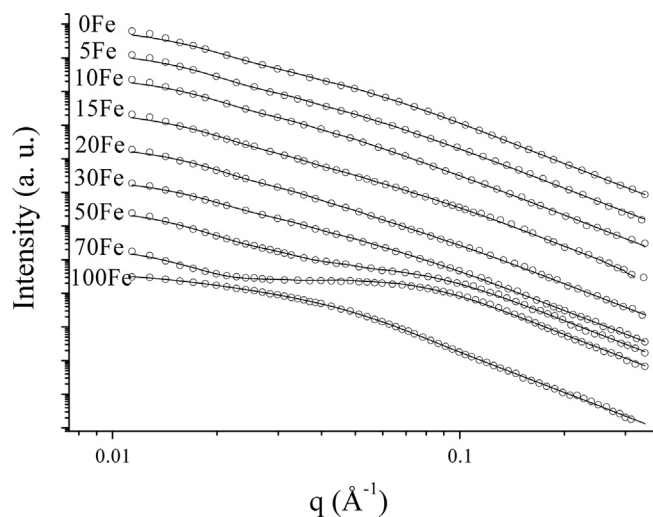


Fig. 3. Small-angle X-ray scattering curves in log-log scale.

590 cm^{-1} . Thus, the presence of hematite related peaks indicates the formation of very well distributed clusters of Fe_2O_3 in samples 15Fe, 20Fe and 30Fe, which were not detected by classic XRD techniques.

4. Discussion

The features of the synthesis method have a strong influence on the specific surface area also affecting both crystallite sizes and agglomeration ratios. The “citrate method” used in this work leads to a nanocrystalline structure because it promotes the formation of many nuclei during the slow dehydration process used to get a gel, which inhibits crystal growth. Heating after dehydration leads to an auto ignition process which proceeds very fast while the flame develops with the liberation of a great volume of gases and reaching very high

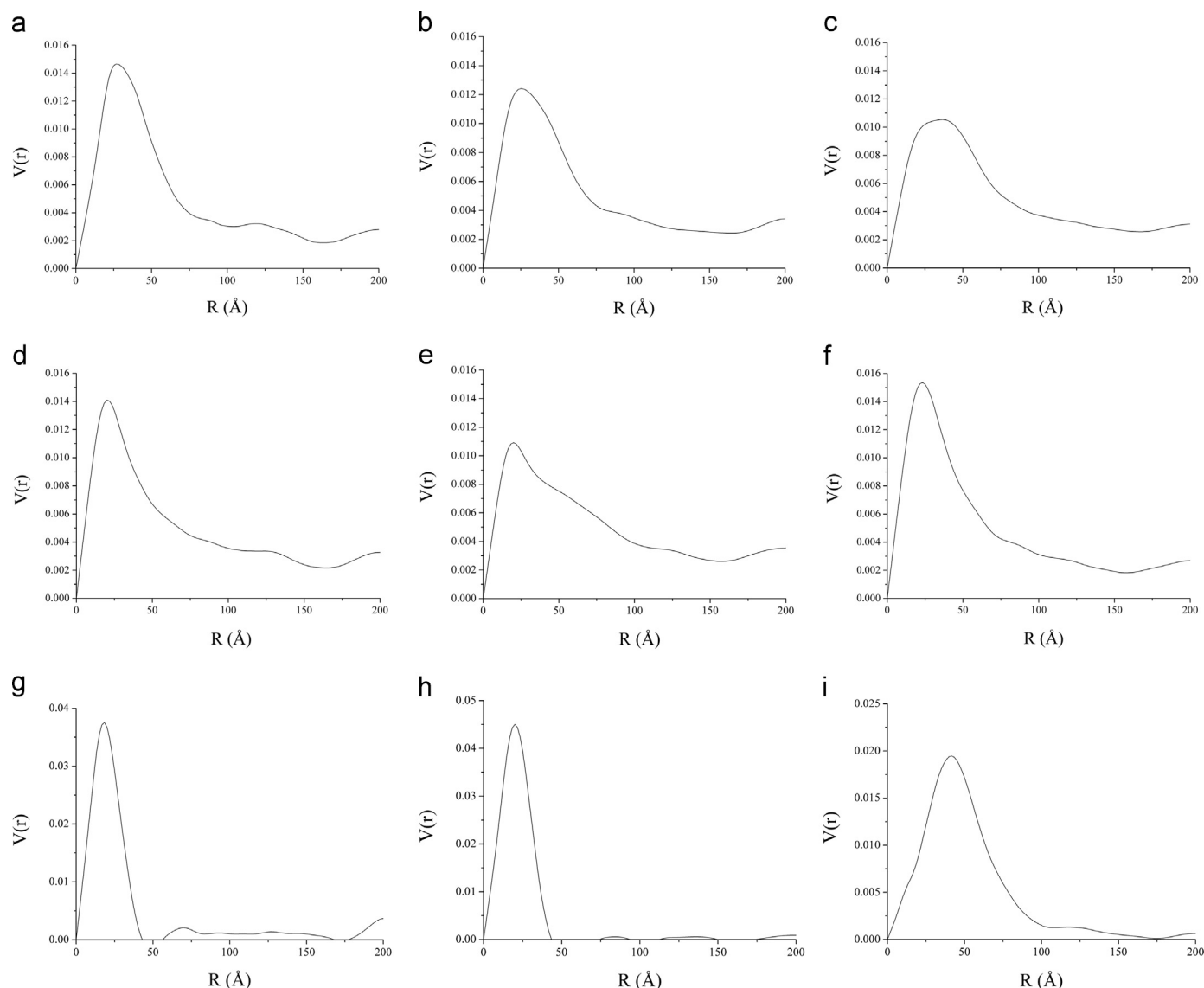


Fig. 4. Volume weighted pore size distributions in the micropore range derived from SAXS experiments. (a) 0Fe; (b) 5Fe; (c) 10Fe; (d) 15Fe; (e) 20Fe; (f) 30Fe; (g) 50Fe; (h) 70 Fe; (i) 100Fe.

temperatures. Ceria containing iron exhibits similar agglomeration ratios but somewhat higher than pure ceria. The observation of agglomeration indicates that each particle is constituted by several crystallites that share their crystalline interfaces.

The variation of the lattice parameter of Ce–Fe solid solutions with iron doping derived from XRD results is displayed in Fig. 6a. As a general trend, a contraction of lattice parameter “*a*” for increasing iron content can be observed, which is a priori expected because cerium cations are substituted by aliovalent iron cations with much lower ionic radii. However, we can notice that the relative variation in lattice parameter “*a*” as increasing iron content from sample

0Fe to sample 30Fe is quite small, i.e. $(\Delta a/a) \sim -0.3\%$, this variation being much lower than that expected from a simple model that only takes into account the ionic radii of Ce^{4+} and Fe^{3+} located in the cation positions in the crystal lattice. Besides, for an increment in iron doping from 10 to 15 at%, the lattice parameter exhibits a clear relative increase (larger than the error bars), while returning to its decreasing trend for further increasing of Fe content, up to 30 at%.

In a recent study of pure ceria nanomaterials by Chen et al. [34] the authors observed an apparent increase of lattice parameters at low crystallite dimensions and discussed the opposite effects of the surface tension that promotes lattice contraction and the non-stoichiometry that induces lattice

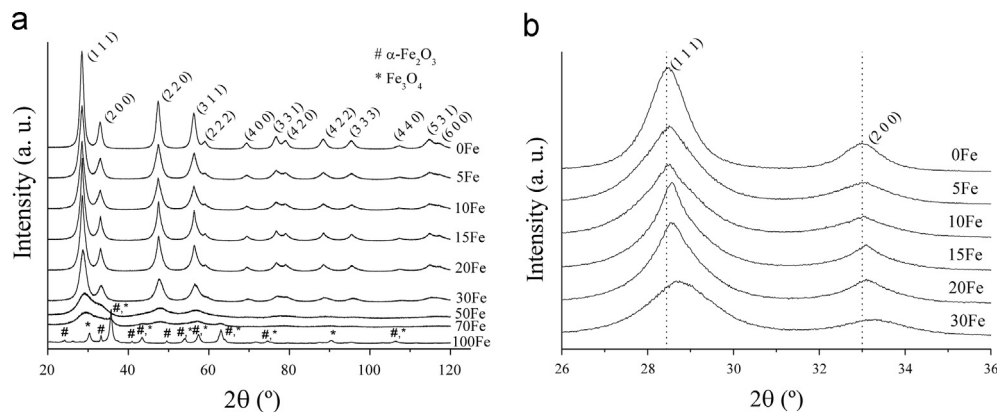


Fig. 5. Powder X-ray diffraction patterns: (a) 2θ range: $20\text{--}120^\circ$; (b) 2θ range: $26\text{--}36^\circ$.

Table 2

Lattice parameter, crystallite size and fitting quality parameter obtained by Rietveld refinement of XRD patterns.

Sample name	Lattice parameter (\AA)	Crystallite size D_{XRD} (nm)	Rwp	Rp	χ^2
0Fe	5.4125(2)	7.1	5.71	3.95	1.33
5Fe	5.4075(3)	5.1	6.15	4.71	1.56
10Fe	5.4057(4)	5.1	6.92	5.44	1.86
15Fe	5.4085(3)	6.1	7.77	6.25	2.31
20Fe	5.4070(4)	5.6	7.46	5.93	2.10
30Fe	5.3987(6)	4.0	6.79	5.09	1.52

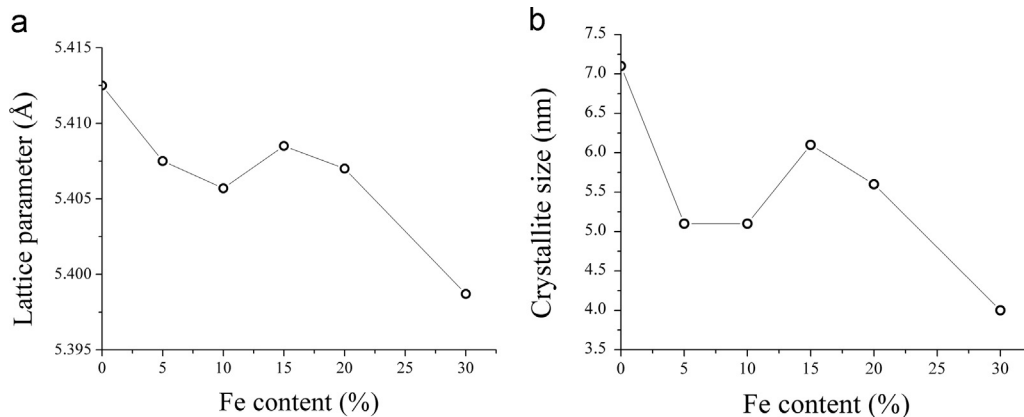


Fig. 6. (a) Refined lattice parameter and (b) average crystallite sizes vs Fe content.

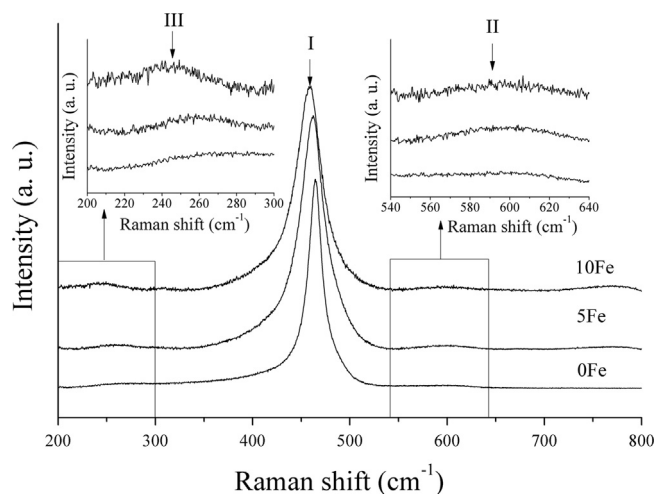


Fig. 7. Raman spectra of samples with low Fe content. Peak I is assigned to F_{2g} Raman active mode in cubic fluorite-like structure. The peaks II and III refer to oxygen-ion vacancies and to a second order transverse mode, respectively.

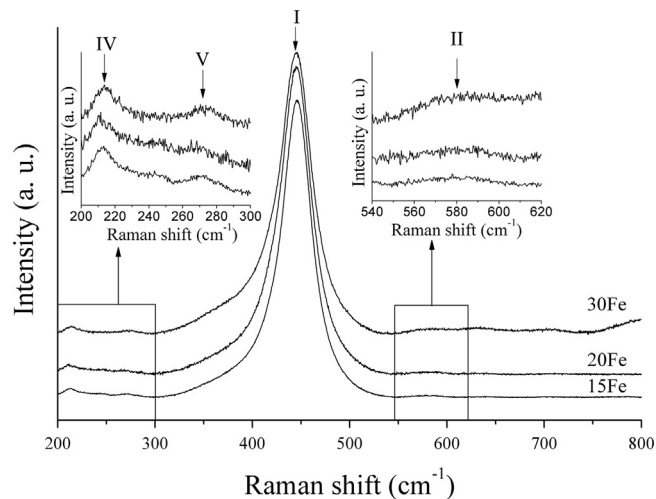


Fig. 8. Raman spectra of samples with high Fe content. Peak I is assigned to F_{2g} Raman active mode in cubic fluorite-like structure. Peak II refers to oxygen-ion vacancies and peaks IV and V to the hematite structure $\alpha\text{-Fe}_2\text{O}_3$.

expansion. These authors [34] concluded that “the contraction effect surpasses the expansion one when the crystallite size reduces from the bulk level to 15 nm, whereas a reverse trend is observed when the size decreases down from 15 to 2 nm”. This results were observed in pure ceria nanocrystals, where the creation of oxygen ion vacancies are associated to reduction of ceria cation from Ce^{4+} to Ce^{3+} with a much higher ionic radius. In our case the incorporation of Fe^{3+} in the lattice structure must create oxygen vacancies when the addition of this aliovalent cation occurs by substitution of Ce^{4+} sites in the host crystal lattice. Therefore, in our case a decreasing trend of the lattice parameter is expected with the non-stoichiometry.

Our Raman results presented in Figs. 7 and 8 show a very low signal related to the formation of oxygen ion vacancies as iron is incorporated in the crystal lattice. The analysis reported

Table 3

Ratios of the areas of Raman peaks at 590 cm^{-1} and 460 cm^{-1} (A_{590}/A_{460}).

Sample	$100 \cdot A_{590}/A_{460}$
5Fe	2.8
10Fe	4.8
15Fe	0.7
20Fe	1.4
30Fe	3.4

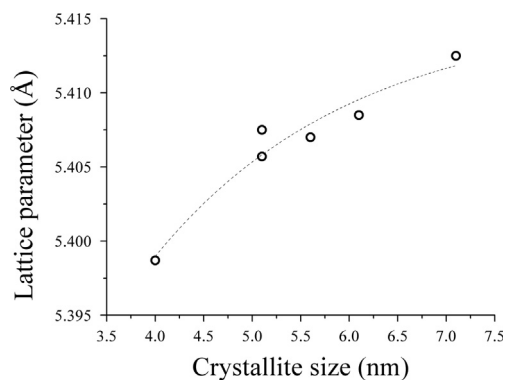


Fig. 9. Dependence of lattice parameter on crystallite average size.

in Table 3 indicates an increment in the A_{590}/A_{460} area ratio as iron doping increases from sample 5Fe to sample 10Fe, nearly duplicating its value, but this ratio almost vanishes for sample 15Fe thus indicating a drastic decrease in oxygen ion vacancy number. This effect is followed by a new increment as iron content increases from 15% to 30%. The area ratios for samples 20Fe and 30Fe are below the values observed for sample 10Fe. Moreover, the formation of iron oxide clusters evidenced by Raman spectra is not high enough to explain the drastic decrease in the number of oxygen vacancies and the expansion in lattice parameter observed for sample 15Fe. Previous researchers have also reported a sudden expansion of lattice parameter above a certain doping value [12,19]. Some of them [12] have proposed a structural model of Fe^{3+} cations occupying either interstitial or substitutional sites in the fluorite structure. Interstitial Fe^{3+} was considered responsible for producing lattice distortions observed as enlarged Ce–O bond lengths. According to our Raman results, the occurrence of some interstitial incorporation of Fe^{3+} cations it is highly probable, which would explain the low variation of lattice parameter and the low signal related to the formation of oxygen ion vacancies. However, average crystallite size exhibits a dependence on iron content very similar to that of the lattice parameter, as it can be verified by comparing the curves displayed in Fig. 6a and b. In Fig. 9 the lattice parameter is plotted as a function of crystallite size. A correlation between the two magnitudes becomes clear. Therefore, the crystallite size, the oxygen ion vacancies and the way the iron is incorporated in the crystal lattice are affecting the lattice parameter values. In order to evaluate the relative contribution of these effects, an additional X-ray diffraction investigation of a series of CeFe solid solutions with same composition and varying average crystallite sizes is required.

5. Conclusions

The citrate synthesis method described here led to the preparation of powdered nanocrystalline materials composed of cerium and iron oxides with different compositions. Samples with iron contents above 30 at% are multiphasic. All mixed Ce–Fe oxides studied in this work (iron content up to 30 at%) are composed of nanometric crystallites but they have different average sizes ranging from 7.1 nm for pure ceria down to 4.0 nm circa for sample 30Fe. The CeFe mixed oxides exhibit a porous structure, with a wide pore size distribution, large specific surface area, and nearly 10% of micropore volume. These textural properties make these nanomaterials good candidates for applications as catalyst support, catalyst, adsorbants, etc.

The lattice parameters of all studied CeFe mixed oxides are lower than that of pure ceria but the observed contraction is much weaker than that expected under the simple assumption of a substitutional incorporation of Fe atoms and combination of Ce–O and Fe–O bond lengths. The analysis by Raman spectroscopy evidenced the formation of a small volume fraction of hematite clusters in samples with relatively high iron content, $x \geq 0.15$ and a low concentration of oxygen vacancies. Therefore, the weak contraction observed on lattice parameter and the low concentration of oxygen vacancies could be a consequence of the competition between interstitial and substitutional incorporations of Fe ions in the ceria host lattice. Likewise, a clear correlation between the oscillatory behavior of the lattice parameter and the similar oscillatory dependence of the crystallite size on iron content was established. This result suggests a rather strong dependence of lattice parameter on nanocrystal size. In order to confirm this statement an additional X-ray diffraction investigation of a series of CeFe solid solutions with same composition and varying average crystallite sizes is required.

Acknowledgements

The PhD scholarship granted to Mariano Mazan by the Fundación Peruihl, Facultad de Ingeniería, Universidad de Buenos Aires (Grant no. Res. CDNo 1958), is gratefully acknowledged. This research received financial support from MINCYT-CAPES BR/11/red/02 (Argentina-Brasil), PIDDEF 011/11 (Argentina) and ANPCyT-PICT 2013 No. 1587.

References

- [1] A. Trovarelli, Structural and oxygen storage/release properties of CeO₂-based solid solutions, *Comment Inorg. Chem* 20 (1999) 263–284.
- [2] M. Radovic, Z. Dohcevic-Mitrovic, A. Golubovic, V. Fruth, S. Preda, M. Scepanovic, Z.V. Popovic, Influence of Fe³⁺-doping on optical properties of CeO_{2-δ} nanopowders, *Ceram. Int.* 39 (2013) 4929–4936.
- [3] S. Tsunekawa, T. Fukuda, A. Kasuya, Blue shift in ultraviolet absorption spectra of monodisperse CeO_{2-x} nanoparticles, *J. Appl. Phys.* 87 (2000) 1318–1321.
- [4] P. Jasinski, T. Suzuki, H.U. Anderson, Nanocrystalline undoped ceria oxygen sensor, *Sens. Actuator B: Chem.* 95 (2003) 73–77.
- [5] J. Marrero-Jerez, S. Larrondo, E. Rodríguez-Castellón, P. Núñez, TPR, XRD and XPS characterisation of ceria-based materials synthesized by freeze-drying precursor method, *Ceram. Int.* 40 (2014) 6807–6814.
- [6] J. Kaspar, P. Fornasiero, M. Graziani, Use of CeO₂-based oxides in the three way catalysis, *Catal. Today* 50 (1999) 285–298.
- [7] Y. Zhang, X. Dou, B. Zhao, M. Yang, T. Takayama, S. Kato, Removal of arsenic by a granular Fe–Ce oxide adsorbent: fabrication conditions and performance, *Chem. Eng. J.* 162 (2010) 164–170.
- [8] F.J. Pérez-Alonso, M. Ojeda, T. Herranz, S. Rojas, J.M. González-Carballo, P. Terreros, J.L.G. Fierro, Carbon dioxide hydrogenation over Fe–Ce catalysts, *Catal. Commun.* 9 (2008) 1945–1948.
- [9] G.K. Reddy, P. Boolchand, P.G. Smimiotis, Sulfur tolerant metal doped Fe/Ce catalysts for high temperature WGS reaction at low steam to CO ratios-XPS and Mössbauer spectroscopic study, *J. Catal.* 282 (2011) 258–269.
- [10] K. Sirichaiprasert, A. Luengnaruemitchai, P. Pongstabodee, Selective oxidation of CO to CO₂ over Cu–Ce–Fe–O composite oxide catalyst in hydrogen feed stream, *Int. J. Hydrog. Energy* 32 (2007) 915–926.
- [11] K. Li, H. Wang, Y. Wei, D. Yan, Partial oxidation of methane to syngas with air by lattice oxygen transfer over ZrO₂-modified Ce–Fe mixed oxides, *Chem. Eng. J.* 173 (2011) 574–582.
- [12] G. Li, R.L. Smith Jr., H. Inomata, Synthesis of nanoscale Ce_{1-x}Fe_xO₂ solid solutions via a low-temperature approach, *J. Am. Chem. Soc.* 123 (2001) 11091–11092.
- [13] A. Laobuthee, C. Veranitisagul, N. Koonsaeng, V. Bhavakul, N. Laosiripojana, Catalytic activity of ultrafine Ce_xGd_ySm_zO₂ synthesized by metal organic complex method toward steam reforming of methane, *Catal. Commun.* 12 (2010) 25–29.
- [14] G. Balducci, J. Kaspar, P. Fornasiero, M. Graziani, M.S.J. Islam, Surface and Reduction Energetics of the CeO₂–ZrO₂ Catalysts, *J. Phys. Chem. B* 102 (1998) 557–561.
- [15] R.D. Shannon, C.T. Prewitt, Effective ionic radii in oxides and fluorides, *Acta Crystallogr. B* 25 (1969) 925–946.
- [16] L. Zhao, S.R. Bishop, J. Hyodo, T. Ishihara, K. Sasaki, XRD and Raman spectroscopy study of Fe solubility in cerium oxide, *ECS Trans.* 50 (40) (2013) 53–58.
- [17] F.J. Pérez-Alonso, M. López Granados, M. Ojeda, P. Terreros, S. Rojas, T. Herranz, J.L.G. Fierro, M. Gracia, J.R. Gancedo, Chemical structures of coprecipitated Fe–Ce mixed oxides, *Chem. Mater.* 17 (2005) 2329–2339.
- [18] G.L. Beausoleil II, A. Thurber, S.S. Rao, G.A. Alanko, C. Hanna, A. Punnoose, Concentration dependence of magnetic moment in Ce_{1-x}Fe_xO₂, *J. Appl. Phys.* 111 (2012) 07B546.
- [19] J. Wang, M. Shen, J. Wang, M. Cui, J. Gao, J. Ma, S. Liu, Preparation of Fe_xCe_{1-x}O_y solid solution and its application in Pd-only three-way catalysts, *J. Environ. Sci.* 24 (2012) 757–764.
- [20] O.H. Laguna, M.A. Centeno, M. Boutonnet, J.A. Odriozola, Fe-doped ceria solids synthesized by the microemulsion method for CO oxidation reactions, *Appl. Catal. B: Environ.* 106 (2011) 621–629.
- [21] H. Lv, H. Tu, B. Zhao, Y. Wu, K. Hu, Synthesis and electrochemical behavior of Ce_{1-x}Fe_xO_{2-δ} as a possible SOFC anode materials, *Solid State Ion.* (2007) 3467–3472.
- [22] K.S.W. Sing, D.H. Everett, R.A.W. Haul, L. Moscou, R.A. Pierotti, J. Roquérol, T. Siemieniowska, Reporting physisorption data for gas/solid systems with special reference to the determination of surface area and porosity, *Pure Appl. Chem.* 57 (1985) 603–619.
- [23] GNOM: Small-angle scattering data processing using the regularisation technique Version 4.6 © ATSAS team 1991–2009.
- [24] D.I. Svergun, Determination of the regularization parameter in indirect-transform methods using perceptual criteria, *J. Appl. Crystallogr.* 25 (1992) 495–503.
- [25] Rodríguez-Carvajal, J. FULLPROF: a program for rietveld refinement and pattern matching analysis, Satellite Meeting on Powder Diffraction of the XV IUCr Congress, 1990, 127.

- [26] B.D. Cullity, Elements of X-Ray Diffraction, Addison Wesley Publishing Company, Reading, Massachusetts, USA, 1956.
- [27] Z. Zhang, D. Han, S. Wei, Y. Zhang, Determination of active site densities and mechanisms for soot combustion with O₂ on Fe-doped CeO₂ mixed oxides, *J. Catal.* 276 (2010) 16–23.
- [28] Q. Shen, G. Lu, C. Du, Y. Guo, Y. Wang, Y. Guo, X. Gong, Role and reduction of NO_x in the catalytic combustion of soot over iron–ceria mixed oxide catalyst, *Chem. Eng. J.* 218 (2013) 164.
- [29] L. Tang, D. Yamaguchi, N. Burke, D. Trimm, K. Chiang, Methane decomposition over ceria modified iron catalysts, *Catal. Commun.* 11 (2010) 1215–1219.
- [30] K. Li, M. Haneda, P. Ning, H. Wang, M. Ozawa, Microstructure and oxygen evolution of Fe–Ce mixed oxides by redox treatment, *Appl. Surf. Sci.* 289 (2014) 378–383.
- [31] D.L. de Faria, S.V. Silva, M.T. de Oliveira, Raman microspectroscopy of some iron oxides and oxyhydroxides, *J. Raman Spectrosc.* 28 (1997) 873–878.
- [32] Y. Wang, F. Wang, Y. Chen, D. Zhang, B. Li, S. Kang, S. Li, L. Cui, Enhanced photocatalytic performance of ordered mesoporous Fe-doped CeO₂ catalysts for the reduction of CO₂ with H₂O under simulated solar irradiation, *Appl. Catal. B-Environ.* 147 (2014) 602–609.
- [33] Q. Wang, X. Li, W. Li, J. Feng, Promoting effect of Fe in oxidative dehydrogenation of ethylbenzene to styrene with CO₂. (I) Preparation and performance of Ce_{1-x}Fe_xO₂ catalyst, *Catal. Commun.* 50 (2014) 21–24.
- [34] L. Chen, P. Fleming, V. Morris, J.D. Holmes, M.A. Morris, Size-related lattice parameter changes and surface defects in ceria nanocrystals, *J. Phys. Chem. C* 114 (2010) 1209–1219.